Research Article | Vol. 29, No. 22 / 25 Oct 2021 / Optics Express 36121
Optics EXPRESS

Surface measuring coherence scanning interferometry beyond the specular reflection limit

MATTHEW THOMAS,[1] RONG SU,[2,*] PETER DE GROOT,[3] JEREMY COUPLAND,[4] AND RICHARD LEACH[1]

[1]Manufacturing Metrology Team, Faculty of Engineering, University of Nottingham, Nottingham NG8 1BB, UK
[2]Shanghai Institute of Optics and Fine Mechanics, Chinese Academy of Sciences, Shanghai 201800, China
[3]Zygo Corporation, Laurel Brook Road, Middlefield, CT 06455, USA
[4]Wolfson School of Mechanical, Electrical and Manufacturing Engineering, Loughborough University, Loughborough LE11 3TU, UK
*surong@siom.ac.cn

Abstract: The capability of optical surface topography measurement methods for measurement of steep and tilted surfaces is investigated through modelling of a coherence scanning interferometer. Of particular interest is the effect on the interference signal and measured topography when tilting the object at angles larger than the numerical aperture slope limit (i.e. the specular reflection limit) of the instrument. Here we use theoretical modelling to predict the results across a range of tilt angles for a blazed diffraction grating. The theoretically predicted interference patterns and surface height measurements are then verified directly with experimental measurements. Results illustrate the capabilities, limitations and modelling methods for interferometers to measure beyond the specular reflection limit.

1. Introduction

Interferometry for surface topography measurement was previously considered to be limited to polished optical surfaces that created simple interference patterns that could be interpreted with fringe tracing or by phase shifting methods. This changed in the 1990s, when it was shown that white light interference microscopy, or more generally, interferometric methods based on optical coherence, could provide meaningful results from rough surface textures [1–3]. The result has been an exponential growth in applications for coherence scanning interferometry (CSI), today serving the needs of many industries that rely on quality control of parts ranging from machined automotive components to additively manufactured parts [4–6].

Qualifying CSI instruments for specific applications often involves an empirical evaluation of measurement capability, such as a gauge repeatability and reproducibility test. Such tests will be part of the toolbox for quality control, but they do not necessarily provide insight into the best configuration of the instrument for a given measurement, nor can they predict how accurate a measurement will be for a specific part type and measurand in advance of exhaustive testing. For this reason, there are on-going efforts to build theoretical models [7–10] that represent the physical principles of measurement well enough to serve as core engines for virtual instruments [11]. These virtual instruments duplicate the response of real instruments with enough confidence to pre-configure an instrument for optimum performance, and to evaluate the associated uncertainty of measurement without a potentially lengthy empirical test. Examples include a recently-developed virtual CSI [11] based on linear three-dimensional (3D) imaging

#435715 https://doi.org/10.1364/OE.435715
Journal © 2021 Received 1 Jul 2021; revised 23 Aug 2021; accepted 24 Aug 2021; published 19 Oct 2021

Optics EXPRESS

theory for surfaces that are continuous and smooth relative to the size of the resolution cell and a CSI model based on a boundary element method (BEM) for modelling instrument response beyond the linear regime, on both smooth and rough surfaces [8].

In recent years, technological enhancements to measurement sensitivity have extended CSI measurement capabilities to parts having surface slope angles that exceed the specular acceptance angle, defined for incoherent microscope illumination by $\theta = \arcsin A_n$, where A_n is the numerical aperture (NA) of the objective. This is a significant next step in the technology, allowing for measurements of spheres, cones and pyramidal structures, even with light directed at near normal incidence, using weakly-reflected light at high scattering angles [12,13]. Reference [14] details the current state of the art and potential of high slope measurement with optical instruments. This new practical capability poses a theoretical challenge for researchers in an applications area where the need is clear: instrument users need to know under what circumstances measurement results for steeply-sloped surfaces are meaningful and have a quantifiable uncertainty. The answer to these questions will be highly dependent on the specific part type and measurement configuration, hence the need for appropriate physical models.

Here we demonstrate the use of the BEM-CSI model [8] on a blazed diffraction grating oriented at various tilt angles, as an informative example case. This object was specifically chosen to represent several aspects of the steep-slope problem, including re-entrant features, a mixture of brightly-reflecting and weakly-scattering surface areas, and a known periodic structure [14]. The BEM-CSI model was chosen as it accounts for multiple scattering and other characteristics of complex surface topography and can use a point cloud representation of the part surface—an essential capability when dealing with re-entrant features. We predict using the model, and then verify experimentally, several characteristics of measurements of our blazed grating, by gradually increasing the tilt angle until the mean plane of the grating exceeds the specular reflection limit determined by the NA of the objective. These results confirm the capability of CSI for measuring steeply-sloped surfaces while clarifying the limitations of the results, leading to greater confidence when using CSI to measure surfaces with complex geometries.

2. Materials and methods

2.1. Modelling methods

In this work, a rigorous CSI model is used to simulate CSI measurements of a blazed grating (described in section 2.2) at different tilt angles (described in section 2.4). The modelling process is illustrated in Fig. 1. In this model, the incident broadband illumination is decomposed into a combination of monochromatic Gaussian beams that illuminate the surface at specific incident angles. For each choice of illumination wavelength and incident angle, scatter is obtained using an algorithm based on BEM for surface scattering [15], and the results of this combined. Following a basic aberration-free imaging process while accounting for the limited NA, a CSI fringe image can be synthesised [8,10].

This 2D model is limited to consider surface profiles and their scatter in the plane of incidence (x-z plane), corresponding to an instrument with a slit pupil. However, the experimental measurement uses an instrument with a circular pupil and illuminates the surface with a right circular cone of illumination. Therefore, to allow for qualitative comparison with experiment, this limitation of our model is mitigated through the measurement of gratings or prismatic surfaces, due to their strong scattering characteristics into the plane into which BEM is limited. As the CSI instrument in our experiment uses circularly polarised illumination with a small radial component also present due to the objective lens' high NA, we consider both s-polarisation and p-polarisation illuminations in our BEM model. The modelling results of the two linear polarisations are displayed separately.

We choose to model the blazed grating profile described in section 2.2, considered in both the L and R cases and across the various tilt angles, as described in section 2.4. Relative to the axis

Optics EXPRESS

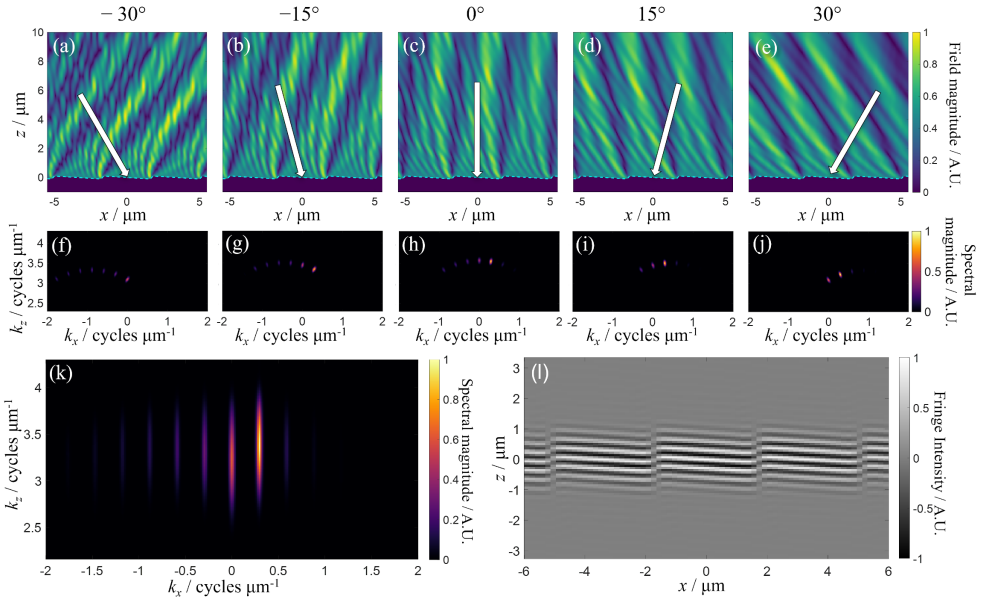

Fig. 1. CSI fringe generation based on a BEM scattering model. (a-e) Scattered field due to monochromatic illumination at different angles, with the incident direction denoted with a white arrow; (f-j) the magnitude of the far-field scatter in K-space for the corresponding incident angles used in (a-e). (k) The combination of K-space results seen in (f-j) but from multiple angles and multiple wavelengths, weighted by the spectral density used, and (l) the ensuing modelled fringes.

along which the pitch and surface width is measured, the longer and shorter facets are inclined at 3.6° and 48.0°, respectively. The modelled profile (Fig. 2) combines the surface texture measured by an atomic force microscope (AFM) along the longer facet with the ideal smooth profile.

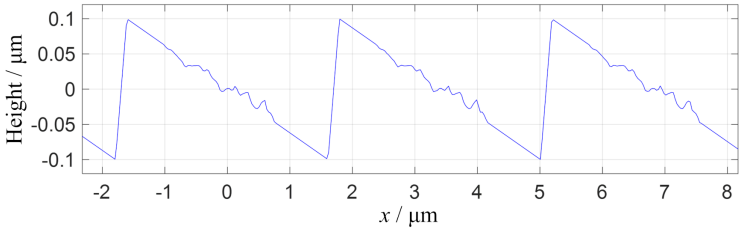

Fig. 2. Geometry of the profile used for modelling, where the central region of each longer facet has had texture, obtained from an AFM measurement, added digitally. Note that the data aspect ratio of the axes is adjusted for easier display.

2.2. *Test samples*

The surface measured is a blazed grating (Thorlabs GR13-0305 visible ruled reflective diffraction grating) with a groove spatial frequency of 300 lines per millimetre. The grating substrate is made of soda lime glass, with an aluminium reflective coating. From the AFM measurement, the grating was found to have a pitch of approximately 3.4 µm, and a peak-to-valley (PV) height of approximately 0.2 µm.

Optics EXPRESS

A periodic grating was chosen for measurement for several reasons. Such surfaces with a single characteristic spatial frequency can be considered as representing one of the many spatial frequency components of a more complex surface. The far-field scatter/diffraction pattern of a grating can be accurately modelled with a variety of methods, and locations of scatter can be predicted analytically. Experimental measurement of a sample at different tilt angles is made much easier with a grating due to the similarity of the surface across the sample, allowing for tilted measurements to be taken from different regions of the sample, rather than creating fiducials visible at any surface tilt angle. The prismatic nature of such surfaces means that for light incident perpendicular to the grooves, the scatter outside the plane of incidence is negligible. This feature allows us to use the 2D BEM surface scattering model to simulate the far-field scatter pattern without significant loss of accuracy. Here, this 2D model corresponds to an 3D optical system with a slit pupil such that the observation can only be made within the plane of incidence, and the illumination is equally limited.

A blazed grating was specifically considered in this work as the asymmetric profile produces asymmetrically distributed scatter patterns. This asymmetry allows us to test the differences in the fringes and topography formed that occur when the surface is tilted, for example, by a constant amount but in each direction. As the scatter is asymmetric, we expect that more scatter and, therefore, more energy would be lost in one of the two cases. Understanding results produced from such a surface is a valuable step towards obtaining and understanding more general results.

2.3. CSI instrument

A commercial CSI instrument with specifications outlined in Table 1 was used for the experimental measurements. A detailed description of the working principle of CSI [16] and recent studies on its 3D surface transfer function can be found elsewhere [10,17–20]. A CSI instrument first acquires 3D fringe data from a surface by taking images over a scan along the optical axis. To this fringe data, a surface reconstruction algorithm is applied, typically taken along the history of each pixel, to calculate the surface topography by using the coherence envelope and/or fringe phase information.

Table 1. Instrument specification

NA	0.55
Acceptance half-angle from arcsin(NA)	33.4°
Field of view (using 1.0× zoom lens)	(0.17 × 0.17) mm
Optical resolution (Sparrow criterion)	0.52 µm
Spatial sampling	0.17 µm/pixel
Illumination central wavelength	~0.56 µm
Illumination full width at half maximum (FWHM)	~0.11 µm

2.4. Experimental methods

The blazed grating is measured with the CSI instrument at different tilt angles, in one of two cases shown in Fig. 3; note that at 0° tilt angle, the L and R cases are mirror images of each other. In this way, the L and R cases indirectly represent a rotation of the grating in both the positive and negative directions. The surfaces are measured in each case at tilt angles between 0° to 50° in increments of 10°.

The fringe data obtained by the instrument is stored as a 3D numerical array. By using a 3D Fourier transform, the fringe spectrum in the spatial frequency domain (K-space) is obtained. The high spatial frequency fringe components that are of interest and contribute to surface

Optics EXPRESS

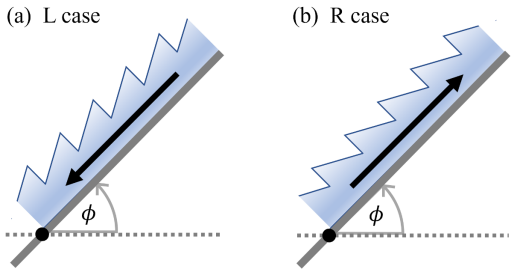

Fig. 3. Diagram presenting the two measurement cases used for measurement of the blazed grating while tilted at angle ϕ, where the black arrow denotes the blaze direction of the grating. (a) L case: the sample is tilted at an angle ϕ with downward facing blaze, (b) R case: the grating is tilted at an angle ϕ with upward facing blaze.

reconstruction are then isolated through application of a band-pass filter (BPF) as described elsewhere [20].

3. Results and discussion

3.1. Fringe generation

The blazed grating in both the L case and the R case are tilted at a range of angles, as previously described in section 2.4, and fringes obtained as a result, displayed in Fig. 4 and Fig. 5. On average, less energy is captured as surface tilt angle is increased [14], with the R case losing more energy compared to the L case as a function of increasing surface tilt angle. To optimise the signal-to-noise ratio for each tilt angle in the experimental case, the illumination light level of the CSI instrument is adjusted for each measurement. Consequently, meaningful comparison between the maximum absolute fringe intensities at different tilt angles is difficult. Therefore, the experimental data has been normalised so that the maximum fringe intensity in each plot is unity. Conversely, as the illumination in the model remains constant, the modelled fringes at all tilt angles can be normalised by the same factor, chosen so that the maximum fringe intensity from the 0° tilt angle case is unity. The scale covered by the greyscale colourmap in each plot shrinks to ensure fringes remain visible, visually obscuring the overall reduction in fringe contrast with increasing tilt angle but emphasising the relative variation in fringe contrast at each tilt angle.

Modelled results using s-polarised and p-polarised illumination are shown in both Fig. 4 and Fig. 5. The results from both polarisation states provide similar qualitative agreement with the experimental result. Visually, the p-polarisation result provides a slightly better agreement. However, given the limited scope of this paper, we have decided to leave the detailed discussion regarding the effects of polarisation to future work. For the L case (Fig. 4), fringes along the longer facets fade out as the surface tilt angle increases, whereas fringe packets, reminiscent of a point spread function (PSF, see Fig. 3 in Ref. [18]), eventually appear at the sharp-edged shorter facets. At 50° tilt angle, these short facets, shorter than half the central wavelength, act as discrete surface points and produce fringes that appear as a tilted train of PSFs. In the R case, seen in Fig. 5, a similar effect is seen; as tilt angle increases, the fringe contrast reduces for the long facets. At 40° and 50°, PSF-like fringes form for the short facets and along the longer facets.

Both the L and R modelling results at 50° tilt angle have reduced fringe contrast from the long surface facets. The long facet has a slope of 54° and 46° for the L50° and R50° case respectively, both exceeding the arcsine of the NA of the instrument (33.4°). Under the Huygens-Fresnel principle, this phenomenon can be understood as each point along the longer facets acting as a

Optics EXPRESS

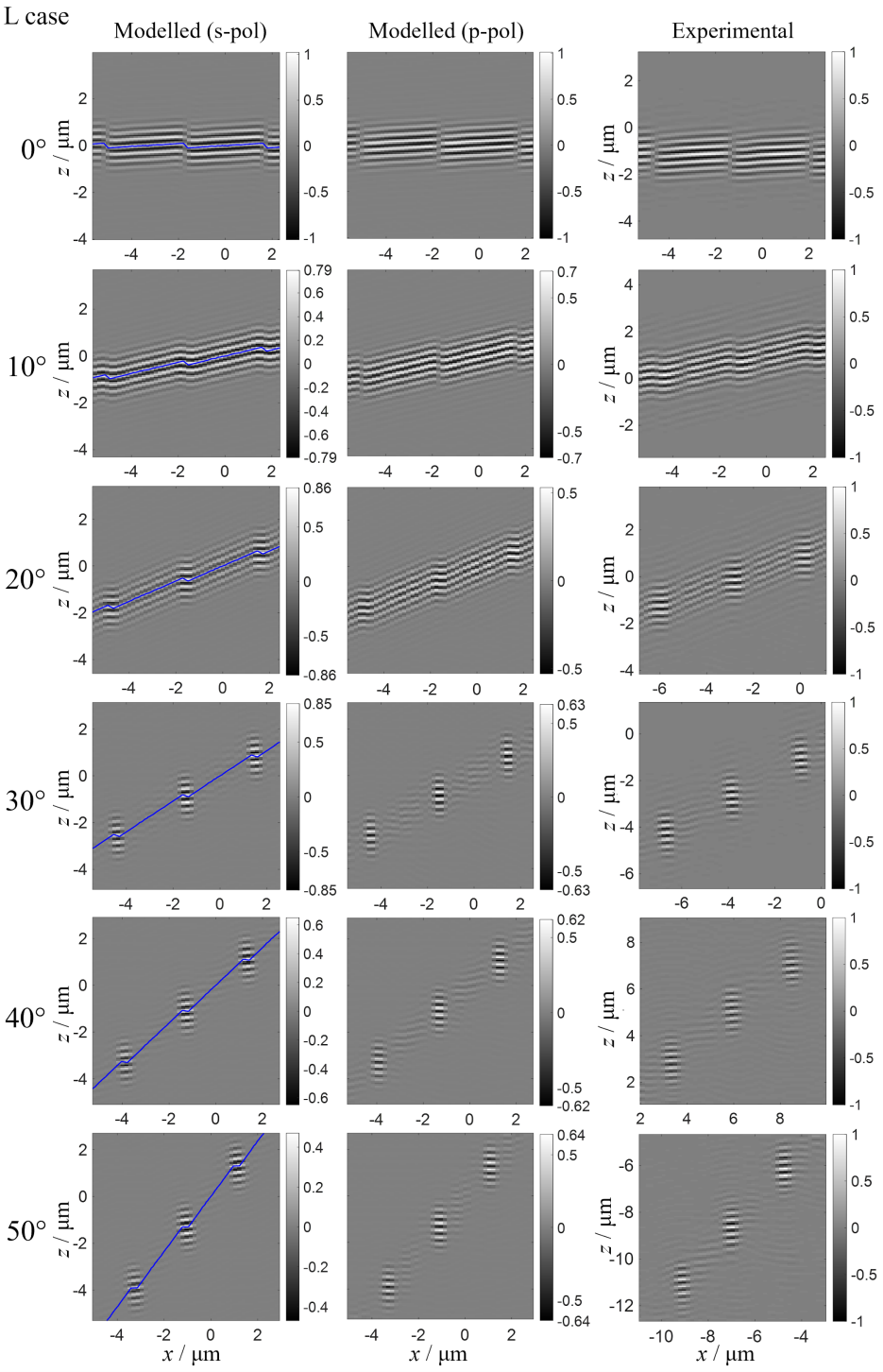

Fig. 4. Modelled (left and middle column) and experimental (right column) fringes of the L case blazed grating at different tilts, where modelled fringes are produced from s-polarisation (left) and p-polarisation (middle) illumination. The solid blue line represents the surface profile used in the model. The grayscale variation represents variation in intensity, with arbitrary units used as described in section 3.1.

Optics EXPRESS

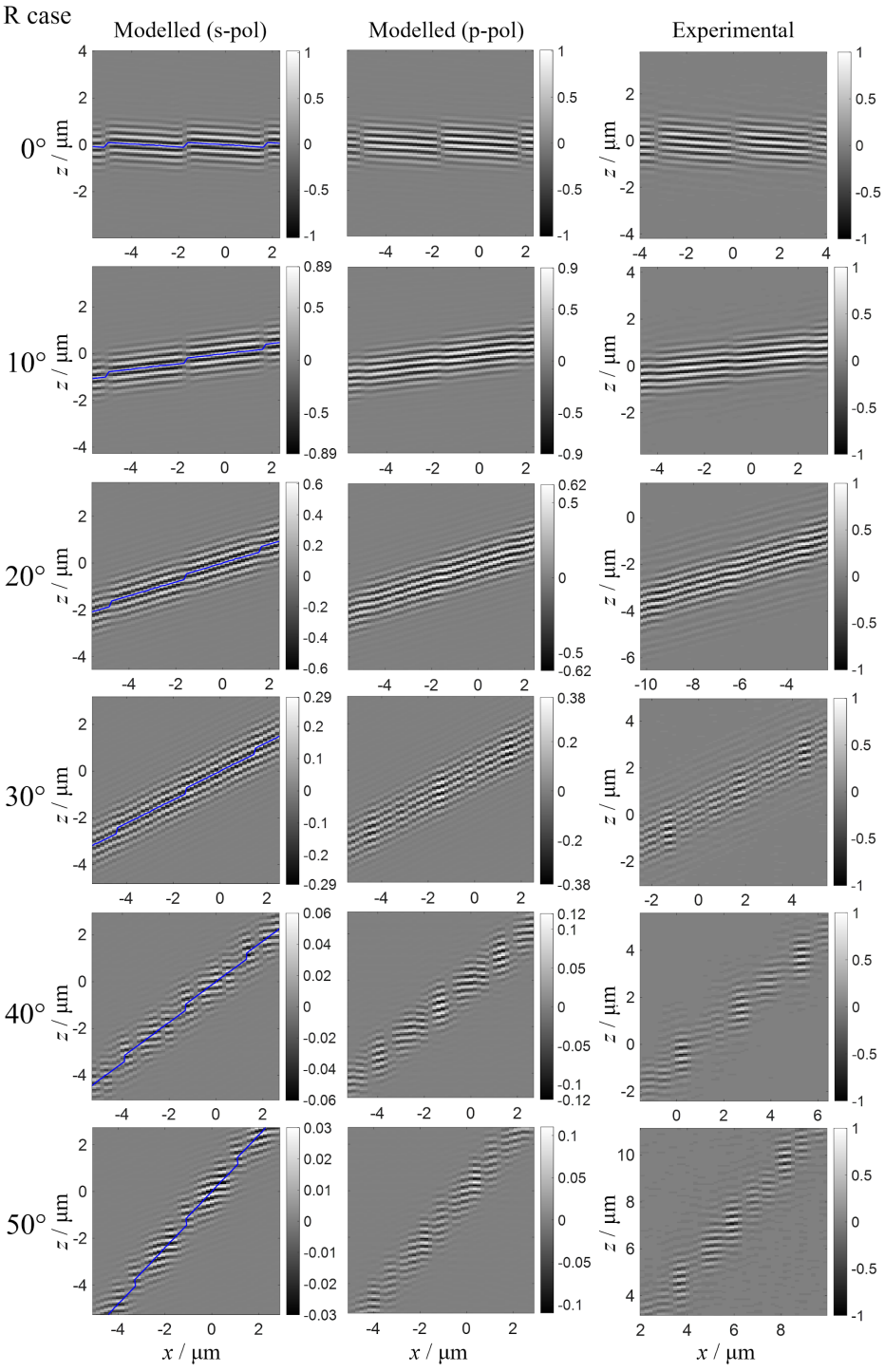

Fig. 5. Modelled (left and middle column) and experimental (right column) fringes of the R case blazed grating at different tilts, where modelled fringes are produced from s-polarisation (left) and p-polarisation (middle) illumination. The solid blue line represents the surface profile used in the model. The grayscale variation represents variation in intensity, with arbitrary units used as described in section 3.1.

Optics EXPRESS

point source, and interfering with each other, such that specular reflection dominates the scatter, causing the majority of the scatter to be lost, and that which is visible appears to be produced by the fine surface texture.

Both the L50° and R50° results also produce PSF-like fringes around the shorter facet. The shorter facets, being only 0.27 µm long, can be considered points of discontinuity on an optical scale for a central illumination wavelength of 0.56 µm. In the L50° case, we can consider them as under-resolved points when illuminated from above, as the shorter facets are almost parallel with the horizontal. In the R50° case, the sharp edge at the junction of the shorter and the longer facets may diffract light back towards the lens. This type of surface discontinuity also produces similar PSF-like fringes. From our modelling result, we can confirm that scatter from high spatial frequency texture along the longer facets will also generate fringes at large surface tilt angles.

As fringe data can be recorded even when all facets have an inclination greater than the acceptance angle, it should be possible to retrieve surface topography with a certain degree of accuracy. Meaningful discussion on the effect of tilt angle on the obtainable surface topography requires consideration of the height estimation process.

3.2. Fringe analysis

Typical surface reconstruction methods rely on evaluating the height at each lateral position, by considering at each camera pixel the interferogram formed along the optical axis over the scanning process. We investigate axial profiles from the modelled profile L50° and R50° case, shown in Fig. 6, and the experimental case, shown in Fig. 7.

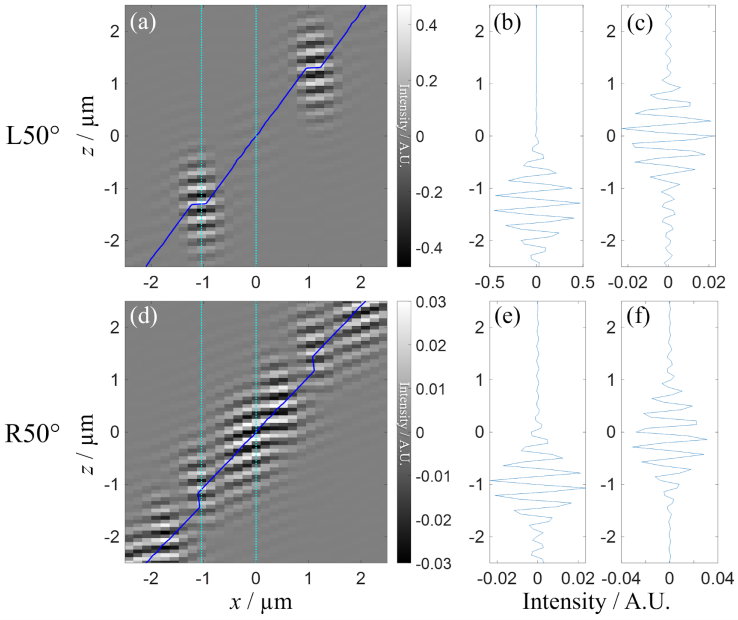

Fig. 6. Modelled fringes from the modelled blazed grating profile tilted at 50° under s-polarisation illumination in the (a-c) L case, and (d-f) the R case. The solid blue line in (a) and (d) represents the surface topography used in the model, while the two dotted cyan lines are the lines along which fringe profiles are obtained. The $x = -1$ µm and $x = 0$ µm profiles are shown in (b,e) and (c,f) respectively. Note the change in intensity range across all plots.

The differences seen between the modelled and experimental fringes, which are larger in the R case, can be attributed to noise present in the experimental measurement, due to the low

Optics EXPRESS

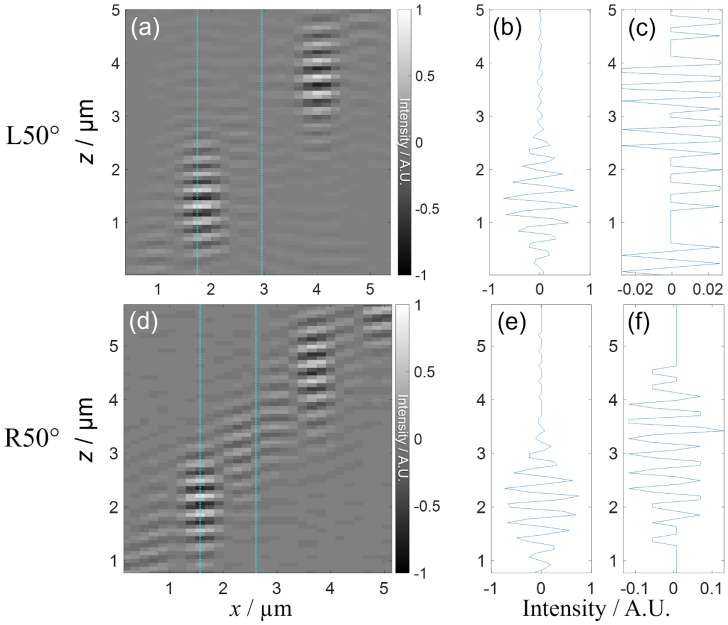

Fig. 7. Experimental fringes from the blazed grating tilted at 50° in the (a-c) L case, and (d-f) the R case. The two dotted cyan lines seen in (a) and (d) are the lines along which fringe profiles are obtained. The left and right profiles are shown in (b,e) and (c,f) respectively. Note the change in intensity range in (c) and (f).

proportion of scattered light captured from the surface. The differences are also likely due to imperfections in the grating, compared to that used in the model, and the inability of our model to fully imitate the actual measurement process (the slit aperture configuration of the model).

The topography obtained from the experimental measurement of the blazed grating tilted at 50° in the L and R cases can be seen in Fig. 8, with results very similar to that of the grating at 45° tilt shown previously in Fig. 5 of [14]. These results use only the coherence profile and do not depend on the phase data present in the fringes.

The original geometry of the blazed grating can be seen in Fig. 8 to mostly be lost. In the L case, this occurs because our shorter facet's width (≈ 0.27 µm) is small enough that the PSF's width for our illumination exceeds it. Therefore, the PSF-fringes provide a false "facet width" dependent primarily on the confidence threshold of our height algorithm; this limitation would occur for any diffraction limited optical system with similar NA and illumination. Depending on the algorithm and confidence threshold chosen, height information may be reported along the magenta lines in Fig. 8(b) through the assumption that the regions of confidence are likely joined by a surface close to a straight line, despite the lack of useful fringe data. This is the cause of the height results reported in Figs. 5(b), 5(e) of Ref. [14]. In the R case, the high spatial frequency micro- and nano-scale surface texture is the source of a significant proportion of the captured scatter, and combined with the low signal-to-noise ratio, and a similar PSF issue, the blazed grating surface structure is almost lost.

Optics EXPRESS

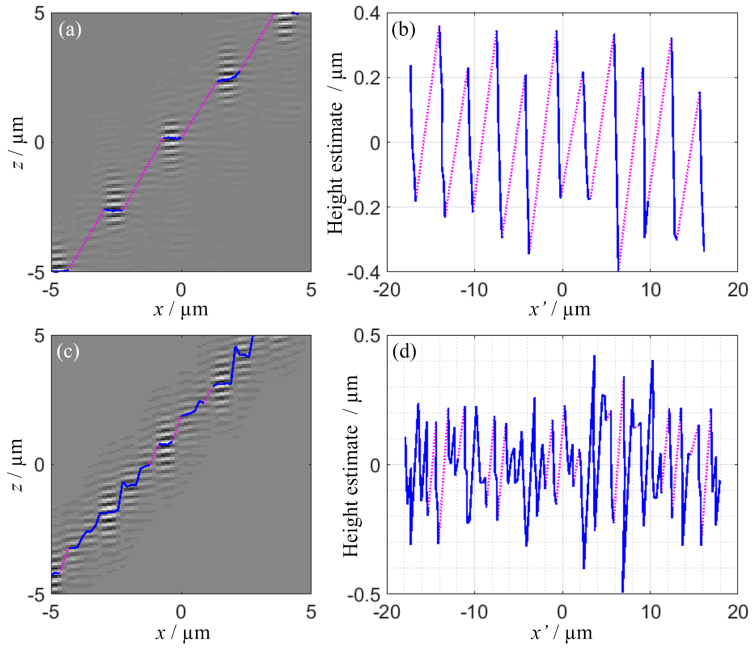

Fig. 8. Topography estimate (coherence profile) obtained from the experimental measurement of the blazed grating tilted at 50° in (a,b) the L case, and (c,d) the R case. The topography with confidence above a set threshold is denoted with the blue solid line, and in regions where height data falls below this threshold a dotted magenta line instead connects with straight lines the regions of confident height data. In (a,c) the topography estimate is displayed on top of the corresponding band-passed fringes, and in (b,d) the topography is rotated 50° to remove the form (levelled).

4. Conclusion

Surface measurement based on optical imaging relies on using an objective lens to collect diffracted or scattered light from the surface of an object. A mirror-like flat surface cannot be measured if the surface is tilted at an angle greater than the specular reflection limit given by the NA because the dominant specular reflected light cannot be collected by the objective lens. To measure a surface tilted beyond the specular reflection limit of the objective lens, the surface must contain structures that cause light to be scattered backwards and collected by the lens. The complex scattering amplitude is then holographically recorded through the 3D interferometric imaging process to generate the 3D fringe data [10] from which surface topography is reconstructed.

We have demonstrated, through BEM-CSI modelling and experimental results, that even when the mean plane of the blazed grating is tilted beyond the NA limit, fringes with the shape of CSI point spread function can be generated due to diffraction and scattering by surface structures such as the sharp edges, local facets smaller or comparable to the optical scale, fine textures, and other surface irregularities. Therefore, despite the loss of specular scatter due to surface tilt, with sufficient micro/nano-scale surface structures, it is possible to obtain useful surface information from the non-specular, backward scattered light.

Funding. Engineering and Physical Sciences Research Council (EP/M008983/1); Horizon 2020 Framework Programme (734174); European Metrology Programme for Innovation and Research (20IND07).

Optics EXPRESS

Acknowledgments. The authors would like to thank Dr Mingyu Liu from the University of Nottingham for the AFM measurement of the blazed grating and to Dr Nikolay Nikolaev from Loughborough University for the use of the BEM code. This work was supported by the Engineering and Physical Sciences Research Council [grant number EP/M008983/1]; the European Union's Horizon 2020 Research and Innovation Programme [grant number 734174]; and the European Metrology Programme for Innovation and Research [grant number 20IND07].

Disclosures. The authors declare that there are no conflicts of interest related to this article.

Data availability. Data available on request.

References

1. T. Dresel, G. Häusler, and H. Venzke, "Three-dimensional sensing of rough surfaces by coherence radar," Appl. Opt. **31**(7), 919–925 (1992).
2. P. J. Caber, "Interferometric profiler for rough surfaces," Appl. Opt. **32**(19), 3438–3441 (1993).
3. P. de Groot, "Principles of interference microscopy for the measurement of surface topography," Adv. Opt. Photonics **7**(1), 1–65 (2015).
4. R. Su, "Coherence scanning interferometry," in *Advances in Optical Surface Texture Metrology*, IOP Series in Emerging Technologies in Optics and Photonics (IOP Publishing, 2020), pp. 2–1–2–27.
5. R. Sachs and F. Stanzel, "Interference Microscopy for Clean Air – How Optical Metrology Is Improving Quality Control of Fuel Injection Systems," in *Fringe 2013: 7th International Workshop on Advanced Optical Imaging and Metrology*, W. Osten, ed. (Springer, 2014), pp. 535–538.
6. C. Gomez, R. Su, A. Thompson, J. DiSciacca, S. Lawes, and R. K. Leach, "Optimization of surface measurement for metal additive manufacturing using coherence scanning interferometry," Opt. Eng. **56**(11), 111714 (2017).
7. T. Pahl, S. Hagemeier, M. Künne, D. Yang, and P. Lehmann, "3D modeling of coherence scanning interferometry on 2D surfaces using FEM," Opt. Express **28**(26), 39807–39826 (2020).
8. M. Thomas, R. Su, N. Nikolaev, J. M. Coupland, and R. K. Leach, "Modeling of interference microscopy beyond the linear regime," Opt. Eng. **59**(03), 1 (2020).
9. J. M. Coupland, R. Mandal, K. Palodhi, and R. K. Leach, "Coherence scanning interferometry: linear theory of surface measurement," Appl. Opt. **52**(16), 3662–3670 (2013).
10. R. Su, J. M. Coupland, C. J. R. Sheppard, and R. K. Leach, "Scattering and three-dimensional imaging in surface topography measuring interference microscopy," J. Opt. Soc. Am. A **38**(2), A27 (2021).
11. R. Su and R. K. Leach, "Physics-based virtual coherence scanning interferometer for surface measurement," Light Adv. Manuf. **2**(1), 1–16 (2021).
12. M. F. Fay, X. Colonna de Lega, and M. Schmidt, "*Measuring high-slope parts using coherence scanning interferometry*," in *Proc. 29th Annual Meeting ASPE* (2014).
13. M. F. Fay, X. Colonna de Lega, and P. de Groot, "Measuring high-slope and super-smooth optics with high-dynamic-range coherence scanning interferometry," in *Classical Optics 2014 (2014)* (Optical Society of America, 2014), p. OW1B.3.
14. M. Thomas, R. Su, P. de Groot, and R. K. Leach, "Optical topography measurement of steeply-sloped surfaces beyond the specular numerical aperture limit," in *Optics and Photonics for Advanced Dimensional Metrology* (International Society for Optics and Photonics (SPIE), 2020), Vol. 11352, p. 1135207.
15. I. Simonsen, "Optics of surface disordered systems. A random walk through rough surface scattering phenomena," Eur. Phys. J. Spec. Top. **181**(1), 1–103 (2010).
16. P. de Groot, "Coherence scanning interferometry," in *Optical Measurement of Surface Topography*, R. K. Leach, ed. (Springer Berlin Heidelberg, 2011), pp. 187–208.
17. R. Su, Y. Wang, J. M. Coupland, and R. K. Leach, "On tilt and curvature dependent errors and the calibration of coherence scanning interferometry," Opt. Express **25**(4), 3297–3310 (2017).
18. R. Su, M. Thomas, M. Liu, J. Drs, Y. Bellouard, C. Pruss, J. M. Coupland, and R. K. Leach, "Lens aberration compensation in interference microscopy," Opt. Lasers Eng. **128**, 106015 (2020).
19. R. Su, M. Thomas, R. K. Leach, and J. M. Coupland, "Effects of defocus on the transfer function of coherence scanning interferometry," Opt. Lett. **43**(1), 82–85 (2018).
20. R. Mandal, J. M. Coupland, R. K. Leach, and D. Mansfield, "Coherence scanning interferometry: measurement and correction of three-dimensional transfer and point-spread characteristics," Appl. Opt. **53**(8), 1554–1563 (2014).